NEOPLASIA
www.neoplasia.com

Volume 14 Number 5 May 2012 pp. 429–439 429

Prevalence of Prostate Cancer Metastases after Intravenous Inoculation Provides Clues into the Molecular Basis of Dormancy in the Bone Marrow Microenvironment[1]

Younghun Jung*,[2], Yusuke Shiozawa*,[2], Jingcheng Wang*, Natalie McGregor†, Jinlu Dai†, Serk In Park*, Janice E. Berry*, Aaron M. Havens*,‡, Jeena Joseph*, Jin Koo Kim*, Lalit Patel†, Peter Carmeliet§, Stephanie Daignault¶, Evan T. Keller†, Laurie K. McCauley*,#, Kenneth J. Pienta†,[3] and Russell S. Taichman*,[3]

*Department of Periodontics and Oral Medicine, University of Michigan School of Dentistry, Ann Arbor, MI; †Departments of Urology and Internal Medicine, University of Michigan Medical School, Ann Arbor, MI; ‡Department of Orthodontics and Pedodontics, University of Michigan School of Dentistry, Ann Arbor, MI; §Laboratory of Angiogenesis & Neurovascular Link, Vesalius Research Center (VRC), VIB, K.U. Leuven, Belgium; ¶Biostatistics Core Facility, University of Michigan Cancer Center, Ann Arbor, MI; #Department of Pathology, University of Michigan School of Medicine, Ann Arbor, MI

Abstract

Bone is the preferred metastasis site of advanced prostate cancer (PCa). Using an *in vivo* murine model of human PCa cell metastasis to bone, we noted that the majority of animals that develop skeletal metastasis have either spinal lesions or lesions in the bones of the hindlimb. Much less frequently, lesions develop in the bones of the forelimb. We therefore speculated whether the environment of the forelimb bones is not permissive for the growth of PCa. Consequently, data on tumor prevalence were normalized to account for the number of PCa cells arriving after intravascular injection, marrow cellularity, and number of hematopoietic stem cell niches. None of these factors were able to account for the observed differences in tumor prevalence. An analysis of differential gene and protein levels identified that growth arrest specific-6 (GAS6) levels were significantly greater in the forelimb *versus* hindlimb bone marrow. When murine RM1 cells were implanted into subcutaneous spaces in immune competent animals, tumor growth in the *GAS6*$^{-/-}$ animals was greater than in *GAS6*$^{+/+}$ wild-type animals. In an osseous environment, the human PC3 cell line grew significantly better in vertebral body transplants (vossicles) derived from *GAS6*$^{-/-}$ animals than in vossicles derived from *GAS6*$^{+/+}$ animals. Together, these data suggest that the differences in tumor prevalence after intravascular inoculation are a useful model to study the molecular basis of tumor dormancy. Importantly, these data suggest that therapeutic manipulation of GAS6 levels may prove useful as a therapy for metastatic disease.

Neoplasia (2012) 14, 429–439

Address all correspondence to: Russell S. Taichman, DMD, DMSc, Department of Periodontics and Oral Medicine, University of Michigan School of Dentistry, 1011 N University Ave, Ann Arbor, MI 48109-1078. E-mail: rtaich@umich.edu

[1]This work is directly supported by the National Cancer Institute (CA163124, CA093900, L.K.M., E.T.K., K.J.P., and R.S.T.), the Fund for Cancer Research (R.T.), the Department of Defense (L.K.M., E.T.K., K.J.P., Y.S., S.I.P., and R.S.T.), and the Prostate Cancer Foundation (K.J.P. and R.S.T.). K.J.P. receives support as an American Cancer Society Clinical Research Professor, National Institutes of Health SPORE in prostate cancer grant P50 CA69568, and the Cancer Center support grant P30 CA46592.

[2]These authors contributed equally as first authors.
[3]These authors contributed equally as senior authors.

Received 12 December 2011; Revised 27 February 2012; Accepted 5 April 2012

Copyright © 2012 Neoplasia Press, Inc. All rights reserved 1522-8002/12/$25.00
DOI 10.1596/neo.111740

Introduction

Prostate cancer (PCa) is the most commonly diagnosed malignancy in US men [1]. Bone is the preferred site of metastasis in advanced PCa and the only clinically evident site of metastasis at the time of death in many individuals [2]. Therefore, there is great need for the development of therapeutic strategies that target advanced PCa and its interactions with bone. A prerequisite for the development of new therapeutics is an improved understanding of the fundamental mechanisms that regulate the metastatic process, including dormancy and growth of tumor cells in bone.

To study bone metastases using human tumor cells, many investigators have turned to an intracardiac injection model in immunodeficient animals [3]. Since the introduction of the model [4], a growing understanding of the initial events that lead to metastases has occurred. The identification of several homing factors [3,5,6], host and tumor-derived factors that are essential for tumor growth in bone [7,8], has been achieved. Hematopoietic stem cells (HSCs) "home" to the bone marrow, as do PCa cells, and compete for occupancy of the HSC niche [9]. One of the molecular determinants for these events, the CXC chemokine stromal–derived factor 1 (SDF-1 or CXCL12) and its receptors, CXCR4 and CXCR7, seem to play pivotal roles in niche competition [5,10]. Once in the marrow, tumor cells engage in cross talk with microenvironmental cells including hematopoietic cells and mesenchymal-derived cells, which activate signaling pathways to establish a vicious cycle of tumor growth and bone remodeling [6].

Whereas intracardiac injection of PCa cells into immune-deficient mice has lead to significant advances in our understanding of the homing and tumor-stromal cross talk, slower progress has been made in understanding the molecular basis of dormancy. Using the intracardiac model, we have noted that most animals that develop skeletal metastasis have either spinal or mandibular lesions or lesions in the bones of the hindlimb. Rarely do lesions develop in the bones of the forelimb. We speculated that there is something unique about these tissues that is not permissive for tumor growth. We used the observed differences in tumor prevalence in the forelimbs *versus* hindlimbs as a model to explore the molecular basis of dormancy from the perspective of the microenvironment.

Materials and Methods

Intracardiac Injections

The PC3 (CRL-1435) PCa cell line was obtained from the American Type Culture Collection (Rockville, MD). Intracardiac injections of luciferase-labeled PC3 cells, $PC3^{Luc}$, were performed in 6- to 8-week-old male Hsd:Athymic Nude-$Foxn1^{nu}$ (Harlan, Haslett, MI), CB.17. SCID, NOD.CB17-*Prkdcscid*/J, or NOD/SCID/IL-$2R\gamma^{null}$ mice (Jackson Laboratory, Bar Harbor, ME) under 3% isoflurane anesthesia (Abbott Laboratories, North Chicago, IL). All the animal experimental procedures were approved by the University of Michigan Committee for the Use and Care of Animals. Left ventricular cardiac injections were performed with 1×10^5 cells suspended in 100 μl of phosphate-buffered saline (PBS) using a 27-gauge needle.

GAS6$^{-/-}$ *Mice*

Homozygous $GAS6^{-/-}$ mice were originally generated by homologous recombination in the laboratory of Dr Carmeliet (University in Leuven) as described [11]. Five- to seven-week-old $GAS6^{-/-}$ mice were used for experimental tumor growth. All experimental procedures were approved by the University of Michigan Committee for the Use and Care of Animals.

In Vivo *Assay of* GAS6$^{-/-}$ *Effect on Subcutaneous Tumor Development*

To evaluate tumor growth, subcutaneous tumors were established. RM1 cells (1×10^4 cells) were mixed in growth factor–reduced Matrigel (Collagen type 1 Rat Tail; BD Biosciences, Bedford, MA). Five- to seven-week-old male C57BL6 background wild-type ($GAS6^{+/+}$) or $GAS6^{-/-}$ mice were anesthetized with isoflurane inhalation. After shaving and cleaning the skin, subcutaneous injections using a 25-gauge needle were used to establish the tumors. The animals were monitored daily, and tumor volumes were evaluated every 3 days, from day 13 to 23. Tumor volumes were calculated using the formula V = the shortest diameter × the longest diameter × height.

Bioluminescence

Tumor incidence was evaluated by bioluminescence imaging (BLI) 4 to 6 weeks after tumor inoculation. Mice were injected intraperitoneally with luciferin (100 μl at 40 mg/ml in PBS) before imaging. Mice were anesthetized with 1.5% isoflurane/air and a Xenogen IVIS (Caliper Life Sciences, Hopkinton, MA) cryogenically cooled imaging system was used. Bioluminescence generated by the luciferin/luciferase reaction served as a locator for cancer growth and was used for quantification using the LivingImage software (Caliper Life Sciences) on a red (high intensity/cell number) to blue (low intensity/cell number) visual scale. A digital grayscale animal image was acquired followed by acquisition and overlay of a pseudocolor image representing the spatial distribution of detected photon counts emerging from active luciferase within the animal. Signal intensity was quantified as the sum of all detected photons within the region of interest during a 1-minute luminescent integration time. Tumor incidence was scored on a dichotomous scale as being either positive or negative if animals had at least one lesion detected in either the humeri or tibial/femur region.

For evaluating of tumor growth of PCa cells in an osseous environment devoid of GAS6, the lumbar vertebrae were isolated from $GAS6^{+/+}$ or $GAS6^{-/-}$ mice 7 days after birth. The vertebrae were sectioned into single vertebral bodies (vossicles). Severe combined immunodeficient (SCID) mice were used as transplant recipients. Four vossicles per mouse were implanted into subcutaneous space. Before implantation, luciferase-labeled PC3 cells ($PC3^{Luc}$) were introduced into vossicles (20,000 cells/10 μl of PBS). Mice were imaged at 2 weeks by BLI.

Disseminated Tumor Cell Quantification by Real-time Polymerase Chain Reaction

The number of disseminated tumor cells (DTCs) in bone was identified using real-time polymerase chain reaction (PCR) [12]. Here, genomic DNA from the designated tissues was isolated using a DNeasy Blood and Tissue Kit (Qiagen, Valencia, CA). Sample concentrations were standardized in each reaction to exclude false-positive results. Real-time PCRs were performed using 15 μl of TaqMan PCR Master mix, 100 nM human Alu TaqMan primers (F – 5′-CAT GGT GAA ACC CCG TCT CTA-3′, R – 5′-GCC TCA GCC TCC CGA GTA G-3′), TaqMan probe (5′-FAM-ATT AGC CGG GCG TGG TGG CG-TAMRA-3′) (Applied Biosystems, Foster City, CA) [13], and 2 μg of isolated tissue DNA in a total volume of 30 μl. The level of expression was detected as an increase in fluorescence using an ABI PRISM 7700 instrument (Applied Biosystems). The DNA levels were expressed as relative copies (% control) normalized against murine β-actin (catalog no. 4331182; Applied Biosystems), and a standard

curve was constructed from serial dilutions of a purified Alu complementary DNA fragment cloned by classic PCR. Numerical data were determined against a standard curve established using murine bone marrow containing log-fold dilutions of human PCa cells. Positive and negative controls included tissues obtained from non–PCa-injected mice or DNA derived directly from PCa cells.

Flow Cytometry

For analyzing HSCs from forelimbs and hindlimbs of SCID mice, the bone marrow cells were flushed from the humerus, femur, and tibia. Cells were incubated first with a biotinylated anti-Lineage (CD5, CD45R [B220], CD11b, Gr-1 [Ly- 6G/C], and Ter-119) antibody cocktail (Miltenyi Biotec, Auburn, CA) for 10 minutes at 4°C, then rinsed and stained with an antibody cocktail of APC-anti–stem cell antigen 1 (Sca-1) (clone D7; eBioscience, San Diego, CA), PE/Cy7–anti–c-Kit (clone 2B8; BioLedge, San Diego, CA), PE–anti-CD150 (clone TC15-12F12.2; BioLegend), fluorescein isothiocyanate (FITC)–anti-CD41 (clone MWReg30; BD Biosciences), FITC–anti-CD48 (clone BCM-1; BD Biosciences), and FITC–anti-Biotin antibodies (Miltenyi Biotec) for another 30 minutes at 4°C. HSCs were analyzed on a FACS Vantage dual laser flow cytometer (Becton Dickinson, Franklin Lakes, NJ) by gating on cells that were $CD150^{+}CD41^{-}CD48^{-}$ $Lin^{-}Sca\text{-}1^{+}cKit^{+}$ (termed SLAM HSCs).

For the cell surface expression of AXL, SKY, and MER, RM1 cells were stained with anti-mouse AXL, SKY, and MER antibodies (catalog nos. MAB8541, MAB759, and MAB591; R&D Systems, Minneapolis, MN) or isotype-matched IgG control for 30 minutes at 4°C, and then stained with PE–anti-rat-IgG antibody (catalog no. F0105B; R&D Systems) for another 30 minutes at 4°C. The cell surface expression of AXL, SKY, and MER on RM1 cells were analyzed on a FACS Vantage dual-laser flow cytometer (Becton Dickinson).

RNA Extraction and Real-time PCR

Total RNA was isolated using the RNeasy Mini Kit (Qiagen). First-strand complementary DNA was synthesized in a 20-μl reaction volume using 0.4 μg of total RNA. Reverse transcriptase products were analyzed by real-time PCR in TaqMan Gene Expression Assays (Applied Biosystems). TaqMan gene expression assays were used for detection of SDF-1, Annexin II (anxa2), TGF-β1, IL15, CCL2, GAS6, AXL, SKY, MER, and β-actin (FAM/MGB probes; Applied Biosystems). The second-step PCRs were run for 40 cycles (95°C for 15 seconds and 60°C for 1 minute) after an initial single cycle of 50°C for 2 minutes and 95°C for 10 minutes. The PCR product was detected using an ABI PRISM 7700 instrument (Applied Biosystems). RNA quantity (C_R) was normalized to the housekeeping gene *β-actin* control by using the formula $C_R = 2^{(40 - \text{Ct of sample}) - (40 - \text{Ct of control})}$. The threshold cycle ($C_t$) is the cycle at which a significant increase in fluorescence occurs.

Histology

The humeri and femora of SCID mice that were used for immunostaining were fixed and then decalcified and paraffin embedded. Tissue sections were dewaxed and rehydrated, then blocked with Image-iT FX signal enhancer for 30 minutes, and incubated for 2 hours at room

Table 1. Prevalence of Bone Lesions after Intracardiac Injection.

Tumor Model	Animal Model	*n*	No. Animals with BLI Evidence of Bone Lesions		Tumor Prevalence (%)	
			Forelimb	Hindlimb	Forelimb	Hindlimb
PC3Luc	Hsd:Athymic Nude-Foxn1nu	8	1	2	13	25
PC3Luc	Hsd:Athymic Nude-Foxn1nu	19	1	2	5	11
PC3Luc	Hsd:Athymic Nude-Foxn1nu	11	1	2	5	9
PC3Luc	Hsd:Athymic Nude-Foxn1nu	10	3	5	15	25
PC3Luc	Hsd:Athymic Nude-Foxn1nu	10	1	3	10	30
PC3Luc	Hsd:Athymic Nude-Foxn1nu	18	0	9	0	50
			Predicted Prevalence (95% Confidence Interval)		9 (04-18)	30 (21-41)*
PC3Luc	CB.17 SCID	26	0	5	0	19
PC3Luc	CB.17 SCID	29	1	11	0	38
PC3Luc	CB.17 SCID	54	2	16	4	30
PC3Luc	CB.17 SCID	54	4	16	7	30
PC3Luc	CB.17 SCID	10	0	1	0	10
PC3Luc	CB.17 SCID	10	0	1	0	10
PC3Luc	CB.17 SCID	19	0	4	0	21
PC3Luc	CB.17 SCID	10	1	0	10	0
PC3Luc	CB.17 SCID	10	1	10	10	100
PC3Luc	CB.17 SCID	35	0	4	0	11
			Predicted Prevalence (95% Confidence Interval)		6 (03-10)	26 (20-32)*
PC3Luc	NOD/SCID	50	4	22	8	44
PC3Luc	NOD/SCID	50	3	23	6	46
			Predicted Prevalence (95% Confidence Interval)		7 (03-14)	45 (36-55)*
PC3Luc	NOD/SCID/IL-2Rγnull	29	2	21	7	72
PC3Luc	NOD/SCID/IL-2Rγnull	10	2	10	20	100
PC3Luc	NOD/SCID/IL-2Rγnull	10	0	1	0	10
			Predicted Prevalence (95% Confidence Interval)		10 (03-33)	55 (34-75)*
Predicted Probability of Tumor Across all Animal Models†					**7 (5-10)**	**33 (28-38)**†

Luciferase-labeled human PC3 cells ($PC3^{Luc}$) were injected into the left heart ventricle of immunodeficient mice, and the development of metastases was tracked by BLI imaging up to 6 weeks. Lesions in the forelimb (humerus, radius, and ulna) or hindlimb (femur, tibia, and fibula) regions were scored as either present or absent. Predicted prevalence, 95% confidence intervals, and associated *P* values were generated from the repeated measures logistic model for forelimb and hindlimb prevalence.

*Compare forelimb and hindlimb prevalence within animal model, $P < .05$.

†Overall test of prevalence of tumor compared between forelimb and hindlimb, $P < .0001$.

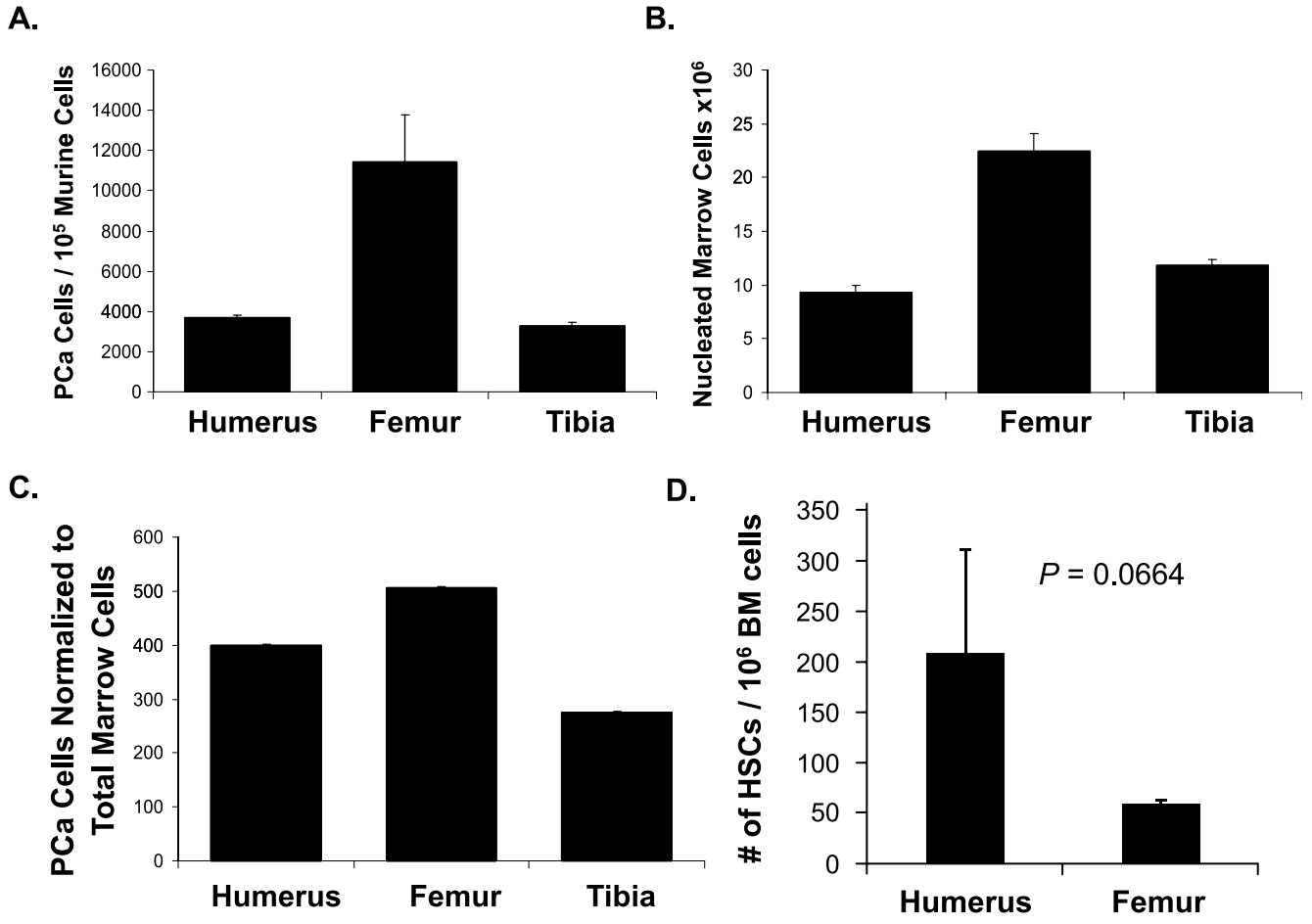

Figure 1. Prevalence of DTCs in murine marrow and relationship to HSC niches. Luciferase-labeled human PC3 cells were injected into the left heart ventricle of immunodeficient mice. (A) At 24 hours later, the number of PCa cells present in the bones was identified using real-time PCR by detecting human Alu sequences and normalized with murine β-actin. Numerical data were established against a standard curve. (B) Total nucleated cells in SCID marrow. (C) Data presented in A normalized by total marrow present in each of the bones (B). Data are presented as mean ± standard deviation. (D) HSC numbers were used to establish an indirect reflection of HSC niche numbers. HSCs were quantified by FACS based on the expression of the SLAM family of receptors $CD150^{+}CD48^{-}CD41^{-}Lin^{-}Sca1^{+}C\text{-}kit^{+}$). Data are presented as mean ± standard deviation.

temperature in the dark with 10 μg/ml primary antibodies combined with reagents of Zenon Alexa Fluor 555(red) labeling kit. Anti-GAS6 antibody (R&D Systems, Minneapolis, MN) or rabbit polyclonal anti–Ki-67 (Abcam) was applied to sections. The antibodies were diluted in PBS plus 0.2% Triton X-100. Sections were postfixed with 10% formalin for 10 minutes followed by processing with ProLong Gold antifade reagent with 4′,6-diamidino-2-phenylindole (DAPI) medium and covered with cover glass. Images were taken with an Olympus FV500 confocal microscope (Olympus, Center Valley, PA).

Apoptosis was evaluated using FragEL DNA Fragmentation Detection Kit (Calbiochem, San Diego, CA). Here tissue slides were deparaffinized and rehydrated and then processed following the manufacturer's instructions. After developing in 3,3′-diaminobenzidine tetrahydrochloride solution, slides were rinsed in water and counterstained with methyl green. Slides were then dehydrated in ethanols, dipped in xylene, and mounted in Permount (Sigma-Aldrich, St Louis, MO).

ELISA

An antibody sandwich ELISA was used to evaluate GAS6 expression in the marrow from the forelimbs and hindlimbs of SCID mice and WT mice or GAS6KO mice as a negative control by following the directions of the manufacturer (catalog no. DY986; R&D Systems). Bone marrow extracellular fluids were obtained by flushing humeri, femora, and tibiae with 500 μl of ice-cold PBS, and the supernatant was harvested by centrifugation at 400*g* for 5 minutes. GAS6 levels were normalized to the total cell number.

Statistical Methods

A repeated-measures logistic model was used to find the predicted probabilities of having an arm tumor or a leg tumor. Tumor prevalence is the binary outcome, with limb type and animal model type included as independent covariates. An unstructured correlation was used to account for the repeated measures within the model (i.e., each mouse has tumor incidence for the hindlimb and tumor incidence for the forelimb in the model).

Numerical data are expressed as mean ± standard deviation unless specified otherwise. The prevalence of tumor lesions was also evaluated against the differences in the immunodeficiency of the animal models using a Mantel-Haenszel χ^2 test. For the real-time PCR assays, a

Kruskal-Wallis test and Dunn multiple comparisons tests were used with the level of significance set at $P < .05$.

Vossicle outcomes of bioluminescence, volume, and weight were analyzed using generalized estimating equations to account for the paired experimental design. The correlation structure was assumed to be unstructured and was designed with location of vossicle nested within the mouse. The independent covariate in the model was group type, and comparisons were made between GAS6 KO *versus* wild type.

Unpaired two-tailed Student's *t* tests were used for all other continuous covariate analyses. The *t* tests and nonparametric tests were performed using the GraphPad Instat statistical program (GraphPad Software, San Diego, CA). SAS 9.3 (SAS Institute, Cary, NC) was used for all modeling. Statistical significance was set at $P < .05$.

Results

Prevalence of Bone Lesions

Bone is the preferred metastatic site of advanced PCa. To create bone metastasis, luciferase-labeled human PCa cells ($PC3^{Luc}$) were injected into the left heart ventricle of immunodeficient mice, and the metastases of these cells were followed by BLI imaging over time. Intriguingly, we noticed that the prevalence of lesions in the long bones was not equally distributed; with fewer lesions in the arms (humeri, radius, and ulna) *versus* those observed in the hindlimb region (femur, tibia, and fibula). To formally examine which long bones are the targets of metastases, a retrospective examination across different experiments and murine strains was performed in which we scored as either present or absent animals with lesions in the forelimb or hindlimb region (Table 1). Predicted prevalence and associated *P* values were generated from the repeated measures logistic model for forelimb and hindlimb prevalence. The prevalence of lesions identified in the hindlimb was significantly greater than that observed in the forelimb (Table 1). These data indicate the probability that 7% of the mice would develop a forelimb tumor (95% confidence interval, 5%-10%) and 33% of the mice would develop a hindlimb tumor (95% confidence interval, 28%-38%). The predicted probability of a forearm tumor is significantly less than that of a leg tumor ($P < .0001$).

Our studies were performed in immunodeficient mouse models, including single-gene mutation models such as nude (Hsd:Athymic Nude-$Foxn1^{nu}$), severe combined immunodeficient (CB.17. SCID), nonobese diabetic (NOD.CB17-*Prkdcscid*/J), and strains with targeted deletion of IL-2Rγ^{null} on the NOD/SCID background (NOD/SCID/IL-2Rγ^{null}). These models of increasing immunodeficiency afforded the opportunity to examine differences in tumor prevalence between the different animal models. We observed that the proportion of mice with hindlimb lesions increases with increasing immunodeficiency of the animal (Mantel-Haenszel χ^2, $P = .0018$; Table 1). However, the animal model type did not demonstrate different probabilities of developing tumors in the forelimb.

Prevalence of DTCs

A possible reason for the noted differences in tumor prevalence between the bones of the forelimb *versus* those of the hindlimb may be due to the differences in the ability of the tumor cells to traffic in the vasculature. To explore this possibility, intracardiac injection of $PC3^{Luc}$ cells was performed, and 24 hours later, the number of PCa cells present in the bones was identified using real-time PCR. Figure 1*A* demonstrates that within 24 hours, the number of DTCs in the humerus was approximately 25% of the total found in the femur. Because this difference could in part explain the observed differences in tumor incidence reported in Table 1, we next normalized the results against total nucleated marrow cells present in each of the bones (Figure 1*B*). As shown in Figure 1*C*, when normalized to total nucleated marrow cells, the number of DTCs in the hindlimb bones (femur + tibia) was only 1.4-fold greater in number than that in the humerus. Using 1.4-fold to normalize for the differences in cells arriving into the forelimb *versus* the hindlimb bones, the observed incidence in osseous lesions, we would therefore expect ~9% of the animals to have lesions located in their arm. These data suggest that the differences in the prevalence of tumors in the limbs of the animals are not likely due to the differences in tumor cell trafficking or homing to the marrow.

Prevalence of Tumors in Relationship to HSC Niches

Previously, we reported that PCa metastases usurp the HSC homing pathways to establish footholds in the marrow [5]. More recently, we demonstrated that disseminated PCa cells directly compete with HSCs for occupancy of the HSC niche and that increasing/decreasing niche size alters dissemination [9]. Therefore, a second possibility that may explain the observed tumor prevalence could be the number of available HSC niches in the humerus *versus* the femur. Because there is no direct method to identify the number of niches present in any tissue, and bone marrow transplant data suggest that only 1% to 5% of HSC niches are unoccupied at any single time [14], we chose to examine

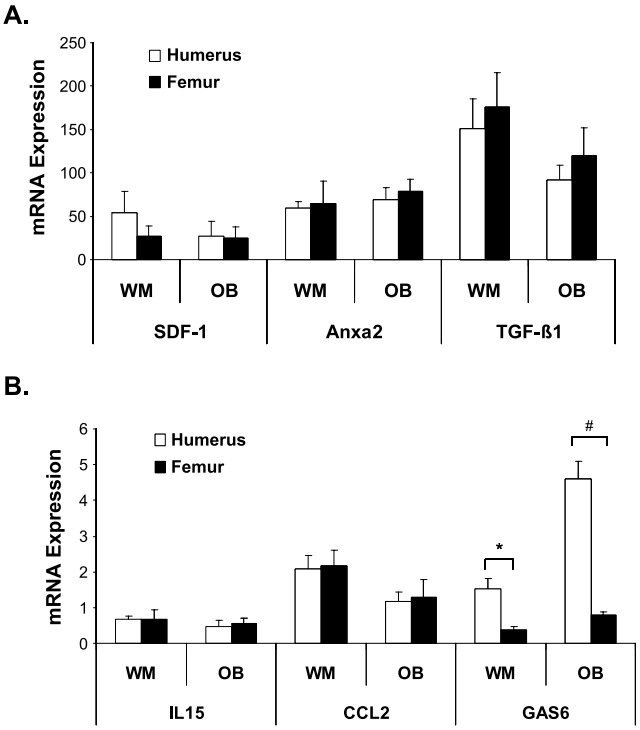

Figure 2. Differential gene expression between the femur and humerus. Real-time PCR for establishing differential mRNA expression for selected genes in the whole bone marrow (WM) or endosteal osteoblasts (OB) isolated by differential digestion from the femur and humerus of SCID mice. (A) Selected gene targets SDF-1, annexin II (anxa2), and TGF-β1. B, Data for IL15, CCL2, and GAS6. Data were normalized to murine β-actin and are presented as mean ± standard deviation from three independent PCRs. $^{*}P < .05$, $^{\#}P < .001$ between paired groups.

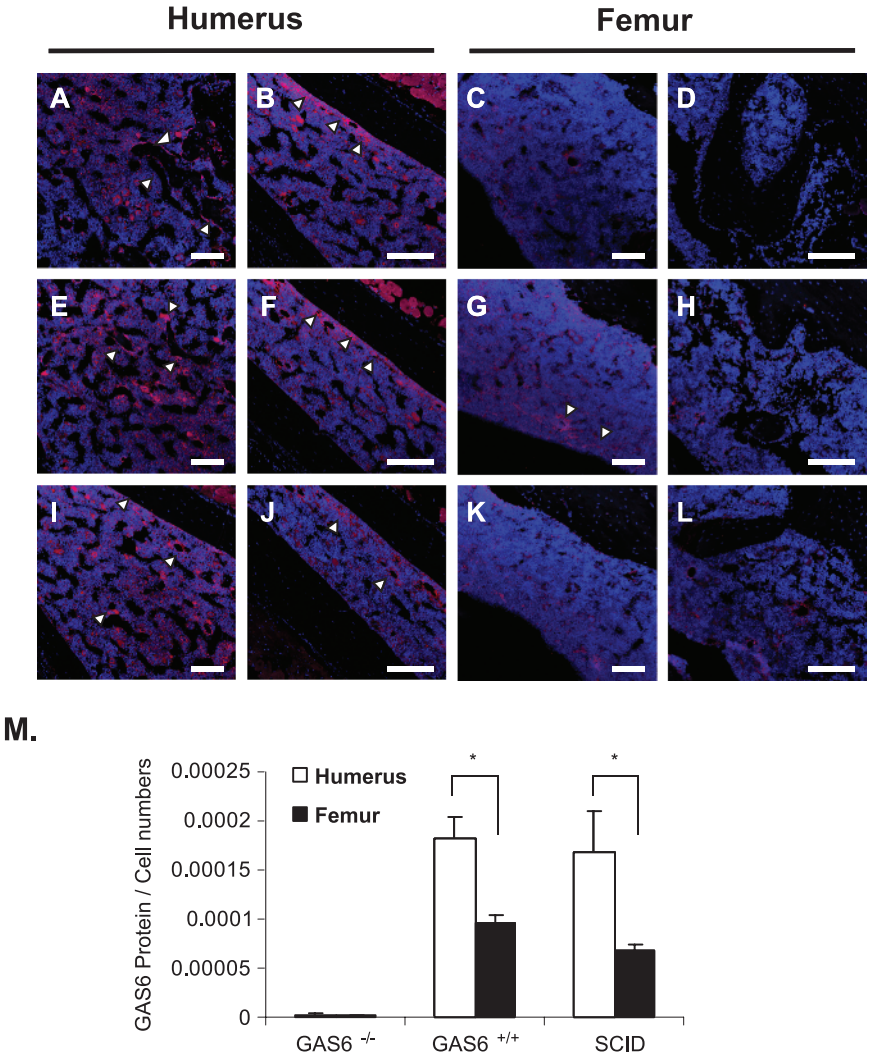

Figure 3. GAS6 protein levels differs between the humerus and femur. (A-L) Representative tissue samples immunostained with anti-GAS6 antibody and counterstained with DAPI nuclear of paired samples from three mice (A-D, E-H, I-L). Original magnification, ×40 (A, C, E, G, I, K) or ×20 (B, D, F, H, J, L). Scale bar, 100 μm. (M) Levels of GAS6 in the extracellular marrow fluids were determined by ELISA normalized by total cell numbers. Data are presented as mean ± standard deviation from triplicate determinations. *$P < .05$ between paired groups.

HSC numbers as an indirect reflection of HSC niche numbers. Here, FACS was used to quantify HSCs using the expression of the SLAM family of receptors as previously demonstrated ($CD150^+CD48^-CD41^-Lin^-Sca1^+C\text{-}kit^+$) [15]. On the basis of this analysis, it was noted that the total number of HSCs in the humerus was ~3.5 times larger than in the femur (Figure 1*D*). Therefore, if the number of HSCs reflects the number of HSC niches, one would expect to observe a greater prevalence of tumors in the forelimbs than in the hindlimbs. Based on this analysis, it seems unlikely that the number of HSC niches alone explains the observed differences in tumor prevalence.

Differential Gene Expression in the Forelimb and Hindlimb Bones

Previous work from our group has demonstrated that endosteal osteoblasts play a significant role in establishing the HSC niche [16–19]. Moreover, it is this niche that is targeted by PCa during metastasis [9]. To explore the molecular mechanisms in tumor prevalence in different bones, whole bone marrow or endosteal osteoblasts were isolated from the humeri, femora, and tibiae of SCID mice, and real-time PCR was performed for selective gene targets. Previously, we have shown that SDF-1 serves a chemoattractant and growth factor for PCa in bone [5,10,20–25], and annexin II (anxa2) serves as an adhesion factor for PCa [26]. Therefore, our initial screen included examinations for SDF-1 and anxa2. There were no differences in messenger RNA (mRNA) expression for SDF-1 or anxa2 between the whole marrow or osteoblasts isolated from the forelimb and hindlimb bones (Figure 2*A*). Similarly, no differences were observed in the expression of TGF-β1, IL15 and CCL2, which were examined owing to their known roles in metastasis and dormancy [7,27–30] (Figure 2, *A* and *B*). In previous studies, we reported that GAS6 inhibits proliferation of PCa cell lines and provides protection from chemotherapy [31]. In addition, GAS6 is a protein known to play a role in suppressing HSC proliferation [32]. Surprisingly, the expression of GAS6 mRNA was significantly greater in both the whole marrow and the osteoblast fractions isolated from the forelimb *versus* those isolated from the hindlimb bones (Figure 2*B*).

GAS6 Expression Differences between Forelimb and Hindlimb Bones

To validate and extend our mRNA expression studies, we explored further if indeed GAS6 protein levels in the humeri were greater than those in the femora and tibiae at the protein level. Here, immunohistochemical staining for GAS6 was performed. We observed that, indeed GAS6 levels were higher in the humeri *versus* the femur bones (Figure 3). Moreover, the staining was localized to the bone surfaces either at trabeculae or at the endosteal surfaces compared to its expression in more central marrow locations (Figure 3, *A-L*). Examination of GAS6 levels in extracellular marrow supernatants further demonstrated that the levels of GAS6 in humerus were greater than those found in the femur (Figure 3*M*).

Growth of PCa Cells in a GAS6-Deficient Environment

If GAS6 limits PCa growth, then PCa cells implanted into *GAS6*$^{-/-}$ animals would be expected to result in the growth of larger tumors

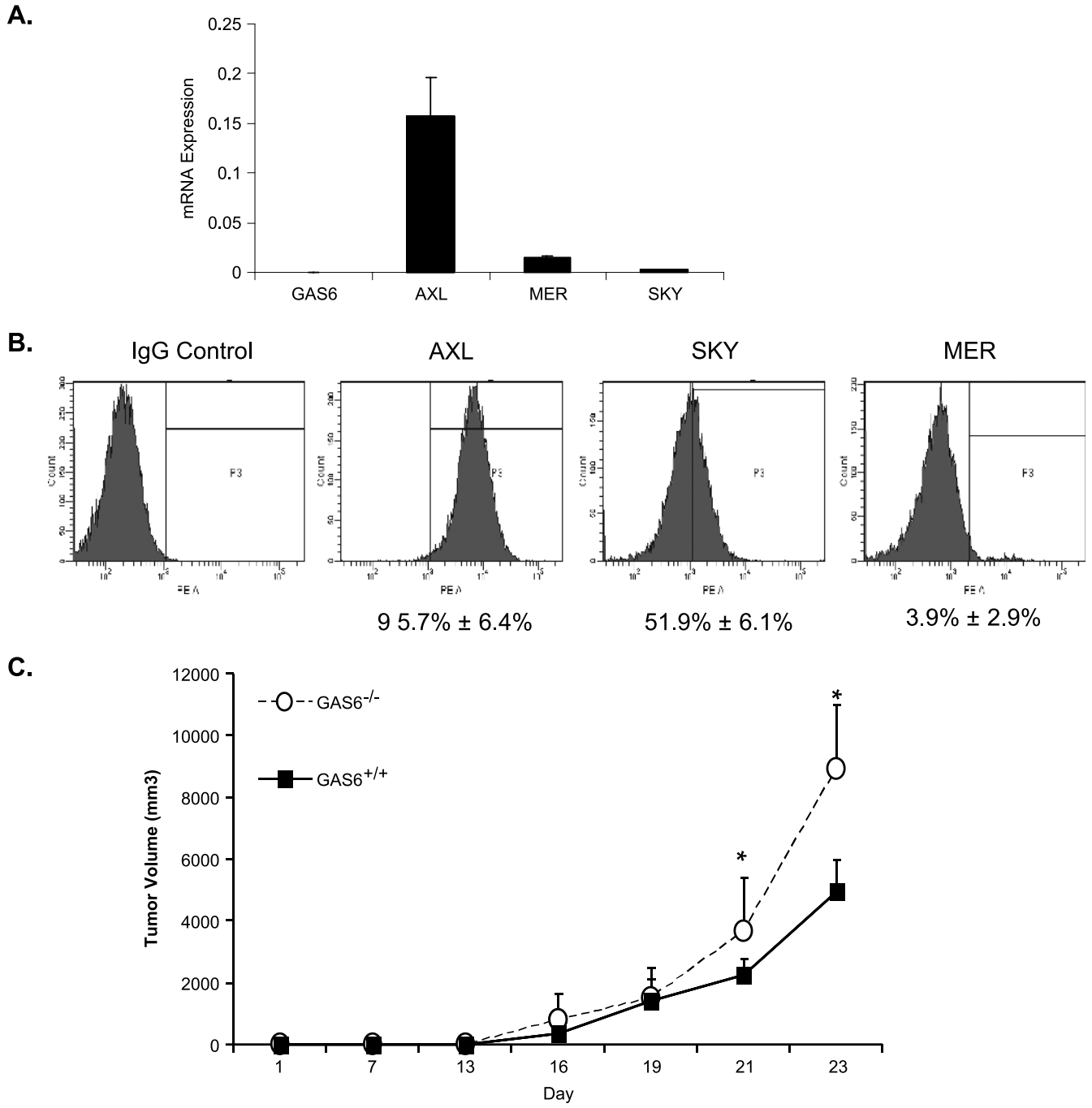

Figure 4. Growth of PCa cells in a GAS6-deficient environment. Expression of GAS6 receptors AXL, SKY, and MER in murine RM1 PCa cells by (A) real-time PCR and (B) FACS. (C) Murine RM1 PCa cells were implanted into *GAS6*$^{+/+}$ or *GAS6*$^{-/-}$ animals, and tumor volume was measured over time by caliper measurements. Data are presented as mean ± standard deviation from triplicate determinations. Differences in growth were noted on days 21 and 23 (*$P < .05$ between paired groups).

compared to tumors grown in wild-type control animals. To test this, murine RM1 PCa cells were first evaluated for their expression of the GAS6 receptors including AXL, SKY, and MER to ensure that GAS6 signaling could occur. Using real-time PCR, AXL expression was significantly higher than MER and SKY, and GAS6 levels were extremely low (Figure 4*A*). At the protein level, AXL expression was also significantly higher than SKY and MER. (Figure 4*B*). Recently *GAS6*$^{-/-}$ animals were generated and made available for experimentation [11]. After validating that these animals do not express GAS6 (Figure 3*M*), we used this model in conjunction with RM1 cells to determine whether GAS6 regulates PCa growth *in vivo*. Critically, when RM1 cells were implanted into the subcutaneous spaces of immune-competent animals, tumor growth in the *GAS6*$^{-/-}$ animals was greater than that in *GAS6*$^{+/+}$ control animals (Figure 4*C*).

Growth of PCa Cells in an Osseous Environment Devoid of GAS6

Our group has developed an osteogenic assay in which neonatal skeletal elements from bone *in vivo* (e.g., vertebral bodies or "vossicles") are used to create an ectopic bone marrow environment where bone niches are generated and can be studied [33]. Here, vossicles from wild-type or *GAS6*$^{-/-}$ neonates were seeded with luciferase expressing cells (PC3^{luc}) and implanted into SCID mice. Over time, tumor growth was evaluated by BLI and by measuring tumor volume and weight. PC3^{luc} cells grew significantly better in vossicles derived from *GAS6*$^{-/-}$ animals compared to tumor cells implanted into vossicles derived from wild-type animals (Figure 5, *A-C*). Ki-67– stained tissues identified more proliferating cells in tumors grown on *GAS6*$^{-/-}$ vossicles *versus* *GAS6*$^{+/+}$ vossicles (Figure 5*D*). At the same time, there was

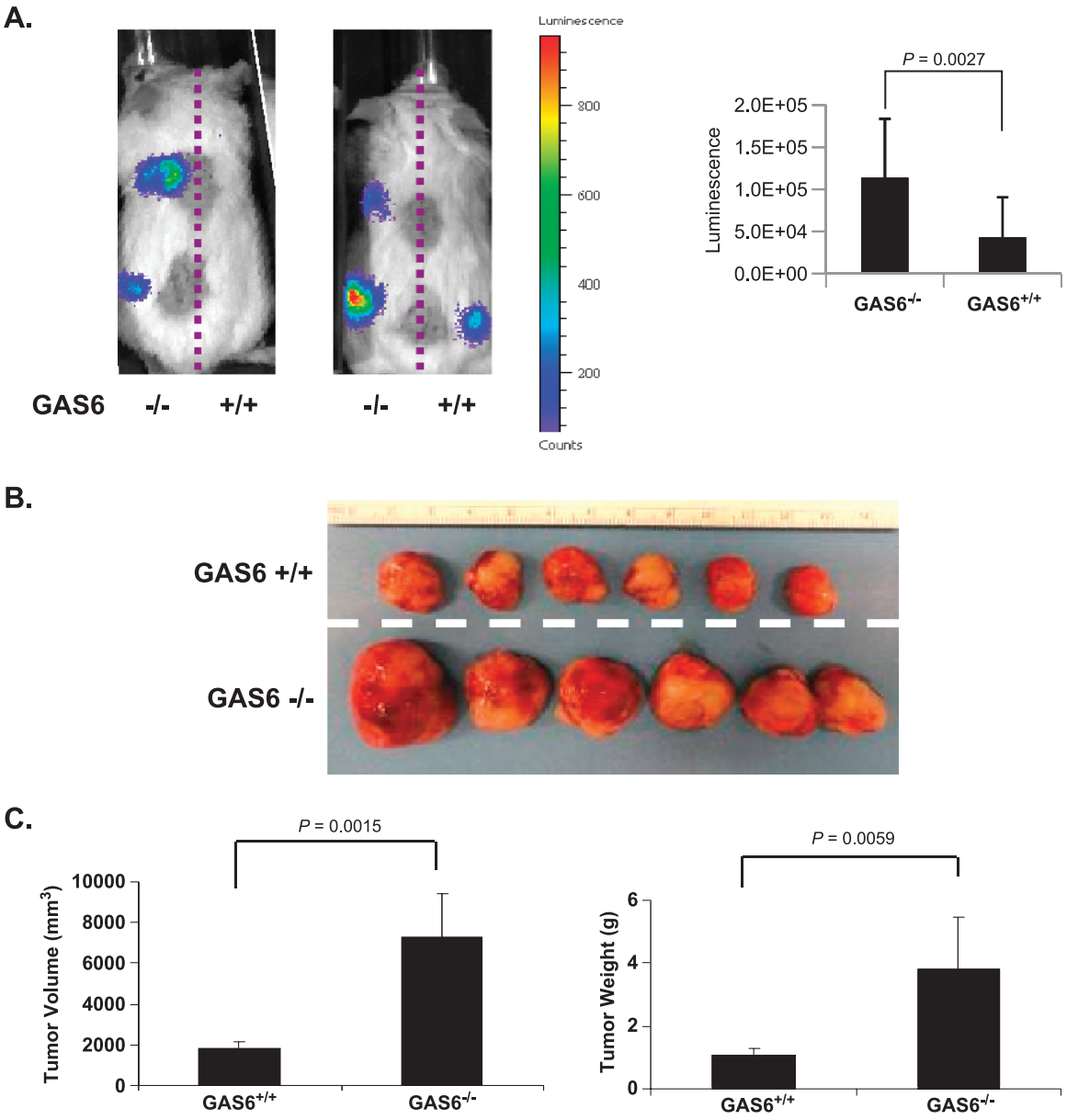

Figure 5. PCa cells grow more rapidly in an osseous environment devoid of GAS6. Paired vossicles from *GAS6*$^{+/+}$ or *GAS6*$^{-/-}$ neonates were seeded with luciferase-expressing cells (PC3^{luc}) and implanted into the backs of SCID mice. (A) Over time, the growth of tumors was evaluated by BLI imaging (left), which was quantified (right). (B) Gross examination of tissues on resection. (C) Tumor volume and weight. Representative tissue samples immunostained for (D) Ki-67 and (E) TUNEL staining. Data are presented as mean ± standard deviation.

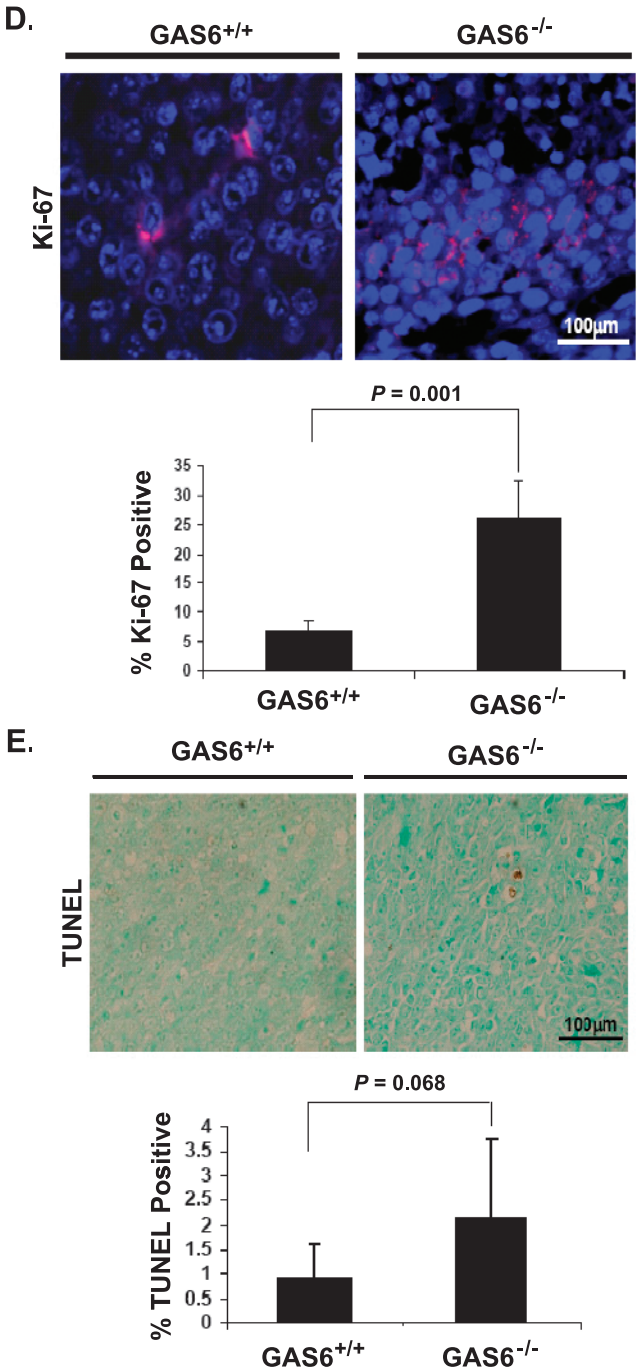

Figure 5. (*continued*).

no significant difference in apoptotic cells in tumor grown in *GAS6*$^{-/-}$ vossicles *versus* *GAS6*$^{+/+}$ vossicles, as determined by TUNEL staining (Figure 5*E*). These observations suggest that the differences in tumor growth arose mostly from an alteration of proliferation rather than changes in apoptosis and further suggest that GAS6 limits tumor cell growth within an osseous environment.

Discussion

The development of PCa disease and its spread to bone remain a major cause of morbidity and mortality in males. Considerable progress has been made in early diagnosis, but once the tumor spreads to distant tissues, survival drastically declines. In 1889, Stephen Paget proposed a "seed-and-soil" metaphor to explain the marked affinity of cancer cells for different tissues: "when a plant goes to seed, its seeds are carried in all directions; but they can only grow if they fall on congenial soil" [34]. More than a century later, the molecular basis for Paget's observations remains unclear. The present work explores the seed-and-soil hypothesis using an animal model of human PCa bone metastasis. Collectively, our group has performed many metastatic assays, and the differences between metastatic lesions found in the forelimbs *versus* the hindlimbs are striking. These differences do not seem to depend on the animal model used. Moreover, the difference seems to be reflected in human disease [35–38]. These observations led us to a more formalized study to determine the molecular basis of the seed and soil hypothesis.

A possible explanation for the observations that fewer lesions are observed in the arms than in the hindlimb regions of mice is based on cardiac output to these regions. This view centers on the "hydrodynamic" or "mechanical" theory that was first proposed by Ewing, which suggested that arterial blood flow was a major determining factor in the frequency of tumor incidence in any given site [39]. Yet surprisingly very little has been published in the context of cardiac output for the appendicular skeleton of a mouse, and even less has been reported in immunodeficient animals. What has been reported has been from studies in rats, where the total cardiac output to the radius, ulna, and humerus is 0.32% ± 0.19% *versus* 0.363% ± 0.27% for the femur and tibia [40]. If these relationships hold for the mouse, then cardiac output is unlikely to account for the prevalence of tumors observed in the present study.

Hematogenous metastases of PCa are known to involve the adhesive interactions between blood-borne tumor cells and the vessel wall. A second possibility therefore is that there may be significant differences in the vasculatures of these regions that permit differential localization of PCa cells. Previous work with intravital microscopy has shown that the microvessels in murine bone marrow including the sinusoids and venules, but not adjacent bone vessels, support rolling interactions of hematopoietic progenitor cells. However, few if any bone-specific differences have been reported [41]. We have shown that PCa cells preferentially bind to bone marrow endothelial cells more than to aortic, umbilical vein, or dermal vascular endothelial cells [42]. Furthermore, PCa cells adhere preferentially to bone endothelial cells and not to extracellular cell matrix proteins present in the bone [43]. Whether these differences can be translated into specific vascular addresses to account for our observations in the forelimb *versus* hindlimb bones remains unclear but seems doubtful because the differences in metastatic lesions are not reflected in the number of PCa cells that actually arrive in the marrow 24 hours after injection [42,44]. Moreover, the possibility that tumor prevalence reflects differences in the number of available HSC niches in the humerus *versus* the femur and tibia seems unlikely. Recently, we demonstrated that disseminated PCa cells directly compete with HSCs for occupancy of the HSC niche and that increasing/decreasing niche size alters dissemination [9]. Although there is no direct method to assess the number of niches present in any tissue, the number of HSCs did not differ significantly between the forelimb and hindlimbs.

Another mechanism that may explain the differences in metastatic prevalence between the forelimb *versus* hindlimb bones is that a factor exists in the bone marrow microenvironment of the hindlimb bones that stimulates growth of the PCa cells compared to the forelimb bones. Conversely, the levels of a suppressive growth factor may be relatively high in the bones of the forelimb *versus* the hindlimb bones. Our search for a stimulatory factor resulted in the identification of

no factor, which was differentially expressed in the hindlimb *versus* the forelimb bones (Pienta et al., unpublished observations). Recently, we showed that GAS6, the ligand for the AXL family RTKs, enhances invasion, inhibits proliferation, prevents apoptosis induced by chemotherapy, and alters cell cycling state of PCa cells [31]. In addition, we demonstrated that activation of AXL by GAS6 on PCa cells in a bone marrow niche environment plays a critical role as a molecular switch to establish dormancy of PCa cells [31]. Surprisingly, we noted that the levels of GAS6 mRNA and protein were significantly higher in the forelimb *versus* hindlimb bones. The reason for this is not clear; however, subcutaneous and intraosseous studies in a GAS6-deficient animal model strongly suggest that GAS6 does limit tumor growth.

The role of GAS6 in PCa is controversial and may reflect activities that are dose and cell maturation dependent, as has been shown for several other ligands including TGF-β1 and PTHrP. Previous reports suggest that GAS6 may be a stimulator of PCa growth [45]. We have made several attempts to replicate these data without success [31], and our more recent *in vivo* data are consistent with a role for GAS6 in limiting PCa growth. However, it is important to keep in mind that the activity of GAS6 is highly dependent on glycosylation and on the cellular context in which the cells find themselves [45,46]. Importantly, there is indeed precedence linking GAS6 or its receptors to tumor promotion [47–50]. It is also important to recognize that the effects of regulatory molecules are often organ and/or dose dependent. For example, parathyroid hormone, although classically reported to be a bone-resorbing hormone, also has anabolic actions in bone by signaling through the same receptor [5]. Likewise, GAS6 may well have growth inhibitory and stimulatory activities in PCa. Further studies using similar models, dosing and protocols are needed before drawing definitive conclusions as to the ultimate effects of GAS6 on skeletal metastases *in vivo*.

Acknowledgments

The authors thank Chris Strayhorn for assistance with the histology. The authors also thank the University of Michigan Flow Cytometry Core and the Imaging Core for their expertise.

References

[1] Walczak JR and Carducci MA (2007). Prostate cancer: a practical approach to current management of recurrent disease. *Mayo Clin Proc* **82**, 243–249.

[2] Taichman RS, Loberg RD, Mehra R, and Pienta KJ (2007). The evolving biology and treatment of prostate cancer. *J Clin Invest* **117**, 2351–2361.

[3] Park SI, Kim SJ, McCauley LK, and Gallick GE (2010). Pre-clinical mouse models of human prostate cancer and their utility in drug discovery. *Curr Protoc Pharmacol* **51**, 14.

[4] Fidler IJ and Nicolson GL (1976). Organ selectivity for implantation survival and growth of B16 melanoma variant tumor lines. *J Natl Cancer Inst* **57**, 1199–1202.

[5] Taichman RS, Cooper C, Keller ET, Pienta KJ, Taichman N, and McCauley LK (2002). Use of the stromal cell–derived factor-1/CXCR4 pathway in prostate cancer metastasis to bone. *Cancer Res* **62**, 1832–1837.

[6] Weilbaecher KN, Guise TA, and McCauley LK (2011). Cancer to bone: a fatal attraction. *Nat Rev Cancer* **11**, 411–425.

[7] Li X, Loberg R, Liao J, Ying C, Snyder LA, Pienta KJ, and McCauley LK (2009). A destructive cascade mediated by CCL2 facilitates prostate cancer growth in bone. *Cancer Res* **69**, 1685–1692.

[8] Thudi NK, Martin CK, Murahari S, Shu ST, Lanigan LG, Werbeck JL, Keller ET, McCauley LK, Pinzone JJ, and Rosol TJ (2011). Dickkopf-1 (DKK-1) stimulated prostate cancer growth and metastasis and inhibited bone formation in osteoblastic bone metastases. *Prostate* **71**, 615–625.

[9] Shiozawa Y, Pedersen EA, Havens AM, Jung Y, Mishra A, Joseph J, Kim JK, Patel LR, Ying C, Ziegler AM, et al. (2011). Human prostate cancer metastases target the hematopoietic stem cell niche to establish footholds in mouse bone marrow. *J Clin Invest* **121**, 1298–1312.

[10] Wang J, Wang J, Dai J, Jung Y, Wei CL, Wang Y, Havens AM, Hogg PJ, Keller ET, Pienta KJ, et al. (2007). A glycolytic mechanism regulating an angiogenic switch in prostate cancer. *Cancer Res* **67**, 149–159.

[11] Angelillo-Scherrer A, de Frutos P, Aparicio C, Melis E, Savi P, Lupu F, Arnout J, Dewerchin M, Hoylaerts M, Herbert J, et al. (2001). Deficiency or inhibition of Gas6 causes platelet dysfunction and protects mice against thrombosis. *Nat Med* **7**, 215–221.

[12] Havens AM, Pedersen EA, Shiozawa Y, Ying C, Jung Y, Sun Y, Neeley C, Wang J, Mehra R, Keller ET, et al. (2008). An *in vivo* mouse model for human prostate cancer metastasis. *Neoplasia* **10**, 371–380.

[13] Lee RH, Hsu SC, Munoz J, Jung JS, Lee NR, Pochampally R, and Prockop DJ (2006). A subset of human rapidly self-renewing marrow stromal cells preferentially engraft in mice. *Blood* **107**, 2153–2161.

[14] Bhattacharya D, Czechowicz A, Ooi AG, Rossi DJ, Bryder D, and Weissman IL (2009). Niche recycling through division-independent egress of hematopoietic stem cells. *J Exp Med* **206**, 2837–2850.

[15] Kiel MJ, Yilmaz OH, Iwashita T, Yilmaz OH, Terhorst C, and Morrison SJ (2005). SLAM family receptors distinguish hematopoietic stem and progenitor cells and reveal endothelial niches for stem cells. *Cell* **121**(7), 1109–1121.

[16] Taichman RS and Emerson SG (1994). Human osteoblasts support hematopoiesis through the production of granulocyte colony-stimulating factor. *J Exp Med* **179**, 1677–1682.

[17] Song J, Kiel MJ, Wang Z, Wang J, Taichman RS, Morrison SJ, and Krebsbach PH (2010). An *in vivo* model to study and manipulate the hematopoietic stem cell niche. *Blood* **115**, 2592–2600.

[18] Taichman RS (2005). Blood and bone: two tissues whose fates are intertwined to create the hematopoietic stem cell niche. *Blood* **105**(7), 2631–2639.

[19] Zhu J, Garrett R, Jung Y, Zhang Y, Kim N, Wang J, Joe GJ, Hexner E, Choi Y, Taichman RS, et al. (2007). Osteoblasts support B-lymphocyte commitment and differentiation from hematopoietic stem cells. *Blood* **109**, 3706–3712.

[20] Wang J, Ying G, Wang J, Jung Y, Lu J, Zhu J, Pienta KJ, and Taichman RS (2010). Characterization of phosphoglycerate kinase-1 expression of stromal cells derived from tumor microenvironment in prostate cancer progression. *Cancer Res* **70**, 471–480.

[21] Wang J, Shiozawa Y, Wang J, Wang Y, Jung Y, Pienta KJ, Mehra R, Loberg R, and Taichman RS (2008). The role of CXCR7/RDC1 as a chemokine receptor for CXCL12/SDF-1 in prostate cancer. *J Biol Chem* **283**, 4283–4294.

[22] Sun YX, Pedersen EA, Shiozawa Y, Havens AM, Jung Y, Wang J, Pienta KJ, and Taichman RS (2008). CD26/dipeptidyl peptidase IV regulates prostate cancer metastasis by degrading SDF-1/CXCL12. *Clin Exp Metastasis* **25**(7), 765–776.

[23] Sun YX, Fang M, Wang J, Cooper CR, Pienta KJ, and Taichman RS (2007). Expression and activation of $\alpha_v\beta_3$ integrins by SDF-1/CXC12 increases the aggressiveness of prostate cancer cells. *Prostate* **67**, 61–73.

[24] Sun YX, Schneider A, Jung Y, Wang J, Dai J, Wang J, Cook K, Osman NI, Koh-Paige AJ, Shim H, et al. (2005). Skeletal localization and neutralization of the SDF-1(CXCL12)/CXCR4 axis blocks prostate cancer metastasis and growth in osseous sites *in vivo*. *J Bone Miner Res* **20**(2), 318–329.

[25] Sun Y-X, Wang J, Shelburne CE, Lopatin DE, Chinnaiyan AM, Pienta KJ, Rubin MA, and Taichman RS (2003). The expression of CXCR4 and CXCL12 (SDF-1) in human prostate cancers (PCa) *in vivo*. *J Cell Biochem* **89**, 462–473.

[26] Shiozawa Y, Havens AM, Jung Y, Ziegler AM, Pedersen EA, Wang J, Wang J, Lu G, Roodman GD, Loberg RD, et al. (2008). Annexin II/annexin II receptor axis regulates adhesion, migration, homing, and growth of prostate cancer. *J Cell Biochem* **105**, 370–380.

[27] Blum DL, Koyama T, M'Koma AE, Iturregui JM, Martinez-Ferrer M, Uwamariya C, Smith JA Jr, Clark PE, and Bhowmick NA (2008). Chemokine markers predict biochemical recurrence of prostate cancer following prostatectomy. *Clin Cancer Res* **14**, 7790–7797.

[28] Wu TG, Perdigao JR, Umhoefer TK, Cao J, Ansari DA, Albrecht TB, Knutson EP, Rose WA, Jorgensen AJ, Ryan LM, et al. (2009). Heterogeneous interleukin-15 inducibilities in murine B16 melanoma and RM-1 prostate carcinoma by interferon-alpha treatment. *J Interferon Cytokine Res* **29**, 719–728.

[29] Salm SN, Burger PE, Coetzee S, Goto K, Moscatelli D, and Wilson EL (2005). TGF-{beta} maintains dormancy of prostatic stem cells in the proximal region of ducts. *J Cell Biol* **170**, 81–90.

[30] Buijs JT, Henriquez NV, van Overveld PG, van der Horst G, ten Dijke P, and van der Pluijm G (2007). TGF-β and BMP7 interactions in tumour progression and bone metastasis. *Clin Exp Metastasis* **24**, 609–617.

[31] Shiozawa Y, Pedersen EA, Patel LR, Ziegler AM, Havens AM, Jung Y, Wang J, Zalucha S, Loberg RD, Pienta KJ, et al. (2010). GAS6/AXL axis regulates prostate cancer invasion, proliferation, and survival in the bone marrow niche. *Neoplasia* **12**, 116–127.

[32] Dormady SP, Zhang XM, and Basch RS (2000). Hematopoietic progenitor cells grow on 3T3 fibroblast monolayers that overexpress growth arrest–specific gene-6 (GAS6). *Proc Natl Acad Sci USA* **97**, 12260–12265.

[33] Koh AJ, Demiralp B, Neiva KG, Hooten J, Nohutcu RM, Shim H, Datta NS, Taichman RS, and McCauley LK (2005). Cells of the osteoclast lineage as mediators of the anabolic actions of parathyroid hormone in bone. *Endocrinology* **146**(11), 4584–4596.

[34] Paget S (1889). The distribution of secondary growths in cancer of the breast. *Lancet* **1**, 571–573.

[35] Rana A, Chisholm GD, Khan M, Sekharjit SS, Merrick MV, and Elton RA (1993). Patterns of bone metastasis and their prognostic significance in patients with carcinoma of the prostate. *Br J Urol* **72**, 933–936.

[36] Ulmert D, Kaboteh R, Fox JJ, Savage C, Evans MJ, Lilja H, Abrahamsson PA, Bjork T, Gerdtsson A, Bjartell A, et al. (2012). A novel automated platform for quantifying the extent of skeletal tumour involvement in prostate cancer patients using the bone scan index. *Eur Urol*. E-pub ahead of print 2012 Jan 27.

[37] Dennis ER, Jia X, Mezheritskiy IS, Stephenson RD, Schoder H, Fox JJ, Heller G, Scher HI, Larson SM, and Morris MJ (2012). Bone scan index: a quantitative treatment response biomarker for castration-resistant metastatic prostate cancer. *J Clin Oncol* **30**, 519–524.

[38] Larson SM, Morris M, Gunther I, Beattie B, Humm JL, Akhurst TA, Finn RD, Erdi Y, Pentlow K, Dyke J, et al. (2004). Tumor localization of 16β-^{18}F-fluoro-5α-dihydrotestosterone *versus* ^{18}F-FDG in patients with progressive, metastatic prostate cancer. *J Nucl Med* **45**, 366–373.

[39] Chambers AF, Groom AC, and MacDonald IC (2002). Dissemination and growth of cancer cells in metastatic sites. *Nat Rev Cancer* **2**, 563–572.

[40] Tothill P (1984). Bone blood flow measurement. *J Biomed Eng* **6**, 251–256.

[41] Mazo IB, Gutierrez-Ramos JC, Frenette PS, Hynes RO, Wagner DD, and von Andrian UH (1998). Hematopoietic progenitor cell rolling in bone marrow microvessels: parallel contributions by endothelial selectins and vascular cell adhesion molecule 1. *J Exp Med* **188**, 465–474.

[42] Lehr JE and Pienta KJ (1998). Preferential adhesion of prostate cancer cells to a human bone marrow endothelial cell line. *J Natl Cancer Inst* **90**, 118–123.

[43] Cooper CR, McLean L, Walsh M, Taylor J, Hayasaka S, Bhatia J, and Pienta KJ (2000). Preferential adhesion of prostate cancer cells to bone is mediated by binding to bone marrow endothelial cells as compared to extracellular matrix components *in vitro*. *Clin Cancer Res* **6**, 4839–4847.

[44] Cooper CR, McLean L, Mucci NR, Poncza P, and Pienta KJ (2000). Prostate cancer cell adhesion to quiescent endothelial cells is not mediated by β-1 integrin subunit. *Anticancer Res* **20**, 4159–4162.

[45] Sainaghi PP, Castello L, Bergamasco L, Galletti M, Bellosta P, and Avanzi GC (2005). Gas6 induces proliferation in prostate carcinoma cell lines expressing the Axl receptor. *J Cell Physiol* **204**(1), 36–44.

[46] Shain SA (2004). Exogenous fibroblast growth factors maintain viability, promote proliferation, and suppress GADD45α and GAS6 transcript content of prostate cancer cells genetically modified to lack endogenous FGF-2. *Mol Cancer Res* **2**(11), 653–661.

[47] van Ginkel PR, Gee RL, Shearer RL, Subramanian L, Walker TM, Albert DM, Meisner LF, Varnum BC, and Polans AS (2004). Expression of the receptor tyrosine kinase Axl promotes ocular melanoma cell survival. *Cancer Res* **64**, 128–134.

[48] Wu YM, Robinson DR, and Kung HJ (2004). Signal pathways in up-regulation of chemokines by tyrosine kinase MER/NYK in prostate cancer cells. *Cancer Res* **64**(20), 7311–7320.

[49] Loges S, Schmidt T, Tjwa M, van Geyte K, Lievens D, Lutgens E, Vanhoutte D, Borgel D, Plaisance S, Hoylaerts M, et al. (2010). Malignant cells fuel tumor growth by educating infiltrating leukocytes to produce the mitogen Gas6. *Blood* **115**, 2264–2273.

[50] Ye X, Li Y, Stawicki S, Couto S, Eastham-Anderson J, Kallop D, Weimer R, Wu Y, and Pei L (2010). An anti-Axl monoclonal antibody attenuates xenograft tumor growth and enhances the effect of multiple anticancer therapies. *Oncogene* **29**, 5254–5264.